Thermal tensor network simulations of the Heisenberg model on the Bethe lattice

Dai-Wei Qu,[1] Wei Li,[1,2,*] and Tao Xiang[3,4,†]

[1]*Department of Physics, Key Laboratory of Micro-Nano Measurement-Manipulation and Physics (Ministry of Education), Beihang University, Beijing 100191, China*

[2]*International Research Institute of Multidisciplinary Science, Beihang University, Beijing 100191, China*

[3]*Institute of Physics, Chinese Academy of Sciences, Beijing 100190, China*

[4]*School of Physics, University of Chinese Academy of Sciences, Beijing 100049, China*

(Received 6 June 2019; revised manuscript received 16 August 2019; published 10 September 2019)

We have extended the canonical tree tensor network (TTN) method, which was initially introduced to simulate the zero-temperature properties of quantum lattice models on the Bethe lattice, to finite temperature simulations. By representing the thermal density matrix with a canonicalized tree tensor product operator, we optimize the TTN and compute accurately the thermodynamic quantities, including the internal energy, specific heat, spontaneous magnetization, etc., at various temperatures. By varying the anisotropic coupling constant Δ, we obtain the phase diagram of the spin-1/2 Heisenberg XXZ model on the Bethe lattice, where three magnetic ordered phases, namely the ferromagnetic, XY, and antiferromagnetic phases, are found in low temperatures and separated from the high-T paramagnetic phase by a continuous thermal phase transition at T_c. The XY phase is separated from the other two phases by two first-order phase transition lines at the symmetric coupling points $\Delta = \pm 1$. We have also carried out a linear spin wave calculation on the Bethe lattice, showing that the low-energy magnetic excitations are always gapped, and find the obtained magnon gaps in very good agreement with those estimated from the TTN simulations. Despite the gapped excitation spectrum, Goldstone-like transverse fluctuation modes, as a manifestation of spontaneous continuous symmetry breaking, are observed in the ordered magnetic phases with $|\Delta| \leqslant 1$. One remarkable feature there is that the transverse correlation length reaches $\xi_c = 1/\ln(z-1)$ for $T \leqslant T_c$, the maximal value allowed on a z-coordinated Bethe lattice.

DOI: 10.1103/PhysRevB.100.125121

I. INTRODUCTION

The Bethe approximation, a renowned cluster mean-field approach proposed by Bethe in 1935 [1], has played an important role in the studies of cooperative phenomena and phase transitions of classical statistical models [2]. This approximation can be rigorously formulated on an ideal lattice of infinite Hausdorff dimension, i.e., the Bethe lattice shown in Fig. 1(a) [3]. The Bethe lattice is also intimately connected with the dynamical mean-field theory [4–6].

A Bethe lattice is a loop-free graph where each site is connected to z neighbors, i.e., z is the coordination number. Figure 1(a), as an example, shows the structure of a $z = 3$ Bethe lattice, whose lattice sites are all equivalent and there exists no boundary on this infinite lattice. This Bethe lattice resembles a two-dimensional honeycomb lattice locally [as emphasized in Fig. 1(b)], but it does not contain any closed loops, e.g., hexagons. A Bethe lattice becomes a Cayley tree if the lattice size is finite, where the sites are arranged in shells around a root site. In stark contrast to the Bethe lattice, there exist boundary sites, which are as many as the bulk sites, on the $z = 3$ Cayley tree.

Tensor networks provide efficient and accurate representations of quantum many-body states both at zero and finite temperatures. The simple update [7], together with many other optimization schemes [8,9], has been widely adopted in the tensor-network simulations of quantum lattice models [10–14]. It has also been shown that the simple update, or more rigorously the canonical tree tensor network (TTN) method, is numerically exact on the Bethe lattice [10]. In addition, the density matrix renormalization group (DMRG) has also been employed to study the magnetic orders and other physical properties of the Heisenberg model on the Cayley tree [15–19]. Besides, the Bethe approximation has also been used in investigating the Fermi-Hubbard systems, where the single-particle Green's function as well as the density of states are calculated [20–22]. However, most of these studies are restricted in the $T = 0$ properties, and there have not been many investigations on the thermodynamic properties of quantum lattice models on the Bethe lattice.

In this paper we extend the TTN approach from zero to finite temperatures and show that it provides an efficient and accurate method to simulate the thermodynamic properties of the Bethe-lattice quantum lattice models. Through the calculations of magnetic order parameters, we obtain the finite-temperature phase diagram of the anisotropic Heisenberg model. Similar as in the two-dimensional honeycomb lattice, three different magnetic ordered phases, i.e., the ferromagnetic (FM), antiferromagnetic (AF), and planar XY

*w.li@buaa.edu.cn
†txiang@iphy.ac.cn

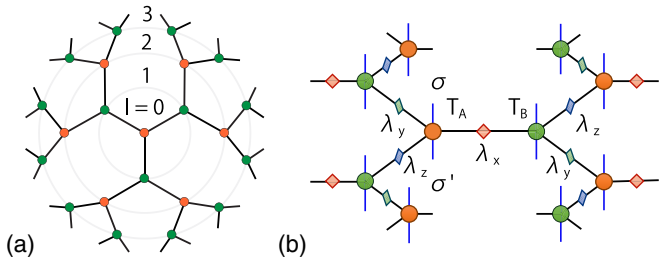

FIG. 1. (a) The $z = 3$ Bethe lattice constitutes an infinite loop-free tree structure. This lattice can be divided into two sublattices, labeled as A (orange circles) and B sublattice (green), respectively. Given a "root" site, the lattice sites on the Bethe lattice can be labeled by the shell number $l = 0, 1, 2, \ldots, \infty$ they reside. (b) A TTN representation of the density matrix, which contains two types of tensors, namely the site tensors T_A and T_B, defined on the lattice nodes. The bond matrices λ_x, λ_y, and λ_z are defined on the corresponding geometric bonds.

phases, are found on the Bethe lattice. The planar XY phase is separated from the FM and AF phases by two first-order phase transition lines at $\Delta = -1$ and 1, respectively, again resembling the two-dimensional case [23].

The correlation length, as shown in Ref. [10], is finite on a Bethe lattice. Here we show that a thermal phase transition can nevertheless happen when the correlation length reaches a "critical" value $\xi_c = 1/\ln(z-1)$ on the Bethe lattice. As revealed by the temperature dependence of thermodynamic quantities in low temperatures, the low-energy excitations of the XXZ model are always gapped. We propose a linear spin wave theory (LSWT) on the Bethe lattice, which gives insight into the low-energy excitations of the system and provides good estimates of the magnon gaps.

The paper is organized as follows. In Sec. II we briefly introduce the Heisenberg XXZ model and the canonical TTN method on the Bethe lattice. The results obtained with this method are presented in Sec. III. In Sec. IV we present a spin wave analysis of the model based on the q representation. Finally, in Sec. V we summarize and discuss about further applications of the method introduced in this work.

II. INTERACTING SPIN MODEL AND TENSOR NETWORK METHOD

A. The Heisenberg XXZ model

The Hamiltonian of the Heisenberg XXZ model reads

$$H = \sum_{\langle i,j\rangle} \left(S_i^x S_j^x + S_i^y S_j^y + \Delta S_i^z S_j^z\right) - h \sum_i S_i^z, \tag{1}$$

where Δ is the anisotropic coupling constant, and $\langle i, j\rangle$ denotes a pair of nearest-neighboring sites. h represents an external magnetic field, which is set as zero if not mentioned explicitly. Note the model with $\Delta = -1$ is equivalent to the isotropic FM Heisenberg model upon a π rotation around the z axis on one of the two sublattices, labeled by green and orange colors in Fig. 1(a), respectively. In the discussions below, we concentrate on the XXZ model defined on a Bethe lattice of coordination number $z = 3$.

B. Canonical TTN representation of the density matrix

As shown in Fig. 1(b), the density matrix on the $z = 3$ Bethe lattice can be expressed as a TTN. A local tensor T defined at a node contains two physical bonds, labeled by σ and σ', representing, respectively, the initial and final states of the density matrix. There are three geometric bonds, labeled by ζ $(=x, y, z)$, through which the network is connected. Besides this, there is also a vector or diagonal matrices λ_ζ defined on each internal bond ζ, whose square (i.e., λ_ζ^2) represents the entanglement spectra between the two blocks that are separated by this bond.

Given a density matrix, its TTN representation is not uniquely determined. By inserting a pair of invertible matrices U and its inverse U^{-1} on each internal bond, we do not alter the density matrix. Nevertheless, the gauge degree of freedom can be fixed by converting a TTN into a canonical form, in which the local tensors T's and diagonal bond matrices λ's satisfy a set of canonical equations. Taking the z bond as an example, the canonical equation is

$$\sum_{x,y=1}^{D} \sum_{\sigma,\sigma'=1}^{d} \lambda_x^2 \lambda_y^2 (T_\alpha^*)_{xyz}^{\sigma\sigma'} (T_\alpha)_{xyz'}^{\sigma\sigma'} = \mathbb{I}_{zz'}, \tag{2}$$

where $\alpha = A$ or B, representing the two sublattices of the $z = 3$ Bethe lattice, $d = 2$ is the dimension of the local basis states of spin-1/2, and $\mathbb{I}$ is a $D \times D$ identity matrix, with D the dimension of the geometric bond. The canonical equations along the x and y bonds can be obtained from Eq. (2) through a cyclic permutation of x, y, and z. This kind of canonical form has already been used in one-dimensional tensor network algorithms, including the density matrix renormalization group (DMRG) [24], time-evolution block decimation [25,26], linearized tensor renormalization group [27,28], etc.

Given an arbitrary TTN representation which generically does not satisfy these canonical equations, we can nevertheless gauge the TTN into the canonical form through a so-called canonicalization procedure elaborated in Appendix A 2.

C. Imaginary-time evolution

The tensor network representation of thermal density matrix $\rho(\beta)$ [27–38] can be determined by taking an imaginary-time evolution, starting from an infinitely high temperature at which $\rho(\beta)$ is represented by the identity operator. This is achieved by taking a Trotter-Suzuki decomposition for the density matrix

$$\rho(\beta) = e^{-\beta H} \approx (e^{-\tau H_x} e^{-\tau H_y} e^{-\tau H_z})^N, \tag{3}$$

$$H_\zeta = \sum_i h_{i,i+\zeta} \quad (\zeta = x, y, z), \tag{4}$$

where $\beta \equiv 1/T$ is the inverse temperature and $\tau = \beta/N$. $h_{i,i+\eta}$ is the interacting Hamiltonian between (nearest-neighboring) sites i and $i + \zeta$ along $\zeta(=x, y, z)$ directions. In practical calculations, the Trotter step τ is set as a small value, e.g., $\tau = 0.01$, to control the Trotter error. For the model we study, all the local terms in each H_η commute with each other, i.e., $[h_{i,i+\zeta}, h_{i',i'+\zeta}] = 0$, thus we can further decompose

$\exp(-\tau H_\zeta)$ into a product of local evolution gates, i.e.,

$$P_\zeta = \exp(-\tau H_\zeta) = \prod_i \exp(-\tau h_{i,i+\zeta}).$$

A detailed introduction to the update scheme of local tensors in the imaginary-time evolution is given in Appendix A 1.

We dub the simple update equipped with the canonicalization procedure (Appendix A 2) as a *canonical* TTN scheme on the Bethe lattice. The canonical TTN approach adopted in the present work indeed improves the accuracy and stability of the calculations, especially for the case with a thermal phase transition, as benchmarked in Appendix A 3.

After obtaining the tensor network representation, to evaluate thermodynamic quantities, we notice that the density matrix operator $\rho(\beta)$ is a product of two half-density matrix operators $\rho(\beta/2)$,

$$\rho(\beta) = \rho(\beta/2)\rho(\beta/2) = \rho^\dagger(\beta/2)\rho(\beta/2). \tag{5}$$

This TTN operator $\rho(\beta/2)$ can be also regarded as a "supervector" $|\rho(\beta/2)\rangle$, defined in the (enlarged) product space of the "ket" and "bra" spaces. In this supervector representation, the partition function then becomes an inner product of $|\rho(\beta/2)\rangle$ and its vector conjugate, namely

$$Z(\beta) = \mathrm{Tr}\rho(\beta) = \langle\rho(\beta/2)|\rho(\beta/2)\rangle. \tag{6}$$

Thus the partition function can be obtained by contracting a bilayer TTN [28].

On the Bethe lattice, contracting the above bilayer supervectors is equivalent to solving the dominant eigenproblem of the transfer tensor M^α defined by

$$M^\alpha_{xx';yy';zz'} = \sum_{\sigma_1,\sigma_2} (T_\alpha)^{\sigma_1\sigma_2}_{xyz}(T^*_\alpha)^{\sigma_1\sigma_2}_{x'y'z'}, \tag{7}$$

whose schematic representation is shown Fig. 2(a). Supposing that X_α, Y_α, and Z_α are the three dominant eigenvectors to find, M^α ($\alpha = A$ or B) simply transfers two of these eigenvectors in one of the sublattice to an eigenvector in the other sublattice, see Figs. 2(b)–2(d). For example, M^B transfers X_A, Y_A to Z_B through the equation [Fig. 2(b)]

$$\sum_{xx'yy'} (X_A)_{xx'}(Y_A)_{yy'}\Lambda_{xx'yy'}M^B_{xx',yy',zz'} = \eta^Z_B(Z_B)_{zz'}, \tag{8}$$

where $\Lambda_{xx'yy'} = \lambda_x\lambda_{x'}\lambda_y\lambda_{y'}$. This defines a generalized eigenvalue problem associated with the transfer tensor M^α and can be solved iteratively, i.e., we start from six random vectors and perform the contractions until all vectors converge.

In stark contrast to the conventional linear eigenvalue problem, there is a gauge flexibility in the definition of eigenvalues η_α here. Once the normalization condition of eigenvectors X_α, Y_α, and Z_α is varied, the corresponding eigenvalues $\eta^{X,Y,Z}_\alpha$ also change, i.e., they are not uniquely defined. In the following we fix the gauge by normalizing all the dominating eigenvectors to 1, e.g., $\|X_\alpha\| = \sqrt{\mathrm{Tr}(X^\dagger_\alpha X_\alpha)} = 1$. This is a convenient choice, and note that once the density matrix $\rho(\beta/2)$ is in the canonical form, cf. Eq. (2), the above iterative contraction procedures can be skipped, since each dominant eigenvector is just identity matrices if represented as a $D \times D$ matrix.

Given the eigenvectors X_α, Y_α, and Z_α, we can evaluate the thermal expectation values of local operators, such as the local

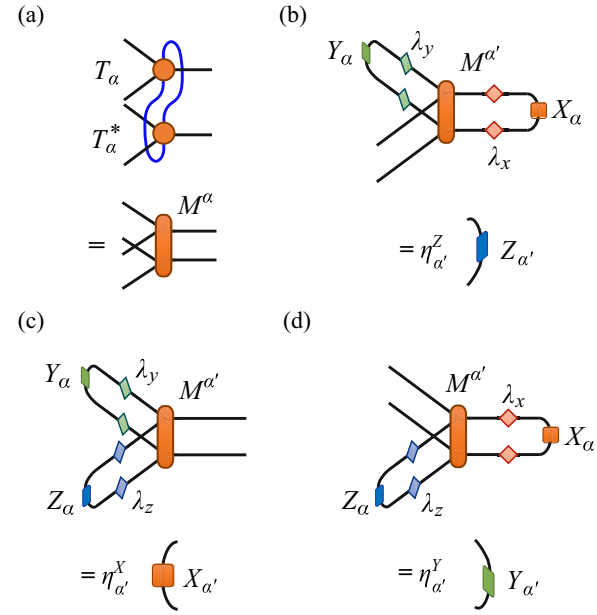

FIG. 2. The generalized eigenvalue problems of transfer tensor M^α. The construction of M^α is illustrated in (a), whose dominant eigenvalues can be obtained through iterative tensor contractions following (b)–(d), see the main text for details.

magnetization. For example, to evaluate the expectation value of an operator $\hat{O}$ on the A sublattice, we first construct the single-site reduced density matrix

$$(\rho_A)_{\sigma_1\sigma_2} = \sum_{xx'yy'zz'\sigma} (X_B)_{xx'}(Y_B)_{yy'}(Z_B)_{zz'} \times (T_A)^{\sigma_1\sigma}_{xyz}(T^*_A)^{\sigma_2\sigma}_{x'y'z'}\lambda_x\lambda_{x'}\lambda_y\lambda_{y'}\lambda_z\lambda_{z'}. \tag{9}$$

The expectation value is then given by

$$\langle\hat{O}\rangle_\beta = \frac{\mathrm{Tr}(\rho_A\hat{O})}{\mathrm{Tr}\rho_A}, \tag{10}$$

which no longer depends on how the generalized dominant eigenvectors are normalized, since ρ_α appears in both the numerator and the denominator. Similarly, we can evaluate the bond energies from the two-site reduced density matrix, etc.

From the canonical TTN, we can also calculate the bipartite-entanglement entropy S_E using the normalized entanglement spectrum λ_ζ, as

$$S_E = -\mathrm{Tr}\left(\lambda^2_\zeta \ln \lambda^2_\zeta\right), \tag{11}$$

which reflects both the quantum entanglement and classical correlations in a thermal equilibrium state. For gapless systems, the entanglement S_E might exhibit a universal logarithmic scaling as a function of temperatures at low T, e.g., in the one-dimensional quantum critical points and two-dimensional Heisenberg models [31,39–42].

Therefore, it is of great interest to explore the scaling behaviors of S_E, particularly near the phase transition temperatures, for the XXZ model on the Bethe lattice. Note, S_E provides a quantitative measure of the bond dimension that is needed for an accurate representation of the thermal density matrix, especially in low temperatures. Generically, the bond dimension D scales exponentially with S_E, which would be

saturated at low temperatures in a gapped system. On the contrary, in a gapless system D would scale algebraically with inverse temperature β, given that $S_E \sim \ln \beta$.

III. NUMERICAL RESULTS

Here we present the thermodynamic results calculated with the canonical TTN method. In our calculations, up to $D = 80$ states are retained in the geometric bonds of local tensors to ensure that the results are converged down to $T = 0.05$.

To benchmark the method, we have evaluated the thermodynamic quantities with the canonical TTN in the classical limit $\Delta = \infty$ [see Eq. (1)], at which the XXZ model is reduced to the exactly soluble Ising model. In this limit, the density matrix has an exact TTN representation with a bond dimension $D = 2$. We find that our numerical results agree excellently with the exact values. One can refer to Appendix B for details. Below we show our TTN results of the quantum XXZ model at finite T.

A. Phase diagram

It has been well established that on a two-dimensional bipartite lattice, say the honeycomb or square lattice, the XXZ model with $-1 \leqslant \Delta \leqslant 1$ breaks the continuous symmetry and possesses a long-range order in the ground state. However, at finite temperatures, the continuous symmetry is restored and the long-range magnetic order is melted by the low-lying excitations according to the Mermin-Wagner theorem [43].

Figure 3 shows the temperature dependence of the magnetic order parameter

$$m = \sqrt{m_x^2 + m_z^2}, \tag{12}$$

where $m_x = \langle S_i^x \rangle_\beta$ and $m_z = \langle S_i^z \rangle_\beta$ are the components within and perpendicular to the XY plane ($\langle S_i^y \rangle_\beta = 0$ by default), respectively. The absolute values of m are the same on the A and B sublattices, and there is no spontaneous symmetry breaking, i.e., $m = 0$, in high temperatures. However, m becomes finite when the temperature drops below a critical value T_c. Particularly, we find that m^2 varies linearly with temperature just below T_c, i.e.,

$$m^2 \propto \frac{T_c - T}{T_c}.$$

We have checked three cases shown in Fig. 3(a) with $\Delta = 0$, 1, and 1.2, which all fall into this scaling in the vicinity of T_c, thus indicating that the transition is mean-field-like.

Figure 4(a) shows the temperature dependence of the specific heat at several different Δ values. A λ-type jump is observed at the critical point T_c, which confirms that the transition from the paramagnetic to magnetic-ordered phase is continuous (though in a mean-field-like fashion). On the other hand, as shown in Fig. 4(b), the entanglement entropy curve vs temperature exhibits a cusp, rather than a diverging peak, at T_c. The absence of divergent S_E at T_c is a natural consequence of the finite correlation length ξ in the system (see discussions on ξ in Sec. III B below). It allows us to perform accurate thermal simulations down to low temperatures $T \leqslant T_c$, by retaining a finite number D of bond states.

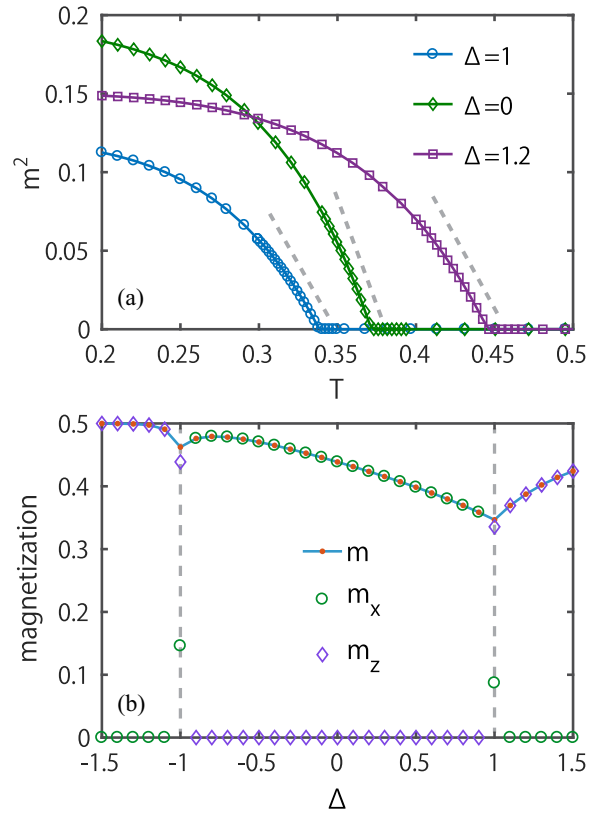

FIG. 3. (a) The spontaneous magnetization of the Bethe-lattice XXZ model, where $m^2 \neq 0$ for $T < T_c$ and vanishes for $T \geqslant T_c$. The dashed lines emphasize a linear relation of m^2 vs T near T_c. (b) The magnetization m and its two components m_x and m_z are plotted vs Δ, at a low temperature $T = 0.125$. The two vertical dashed lines denote the high symmetry points $\Delta = \pm 1$.

Figure 5 shows the T-Δ phase diagram of the Heisenberg XXZ model on the Bethe lattice, where three magnetic ordered phases are observed in low temperatures, by varying the anisotropic parameter Δ. As depicted in Fig. 3(b), for $\Delta > 1$ and $\Delta < -1$, the low-temperature states are AF and FM ordered, respectively. The system spontaneously breaks the Z_2 symmetry, as characterized by $m_z \neq 0$ and $m_x = 0$. When $|\Delta| < 1$, the planar $U(1)$ symmetry is broken, with $m_x \neq 0$ and $m_z = 0$, in low temperatures. This is in stark contrast to the corresponding two-dimensional lattice models with the same Δ parameter, where no long-range order exists at any finite temperature according to the Mermin-Wagner theorem.

On the two vertical phase boundaries (marked by the two dashed lines in Fig. 5), both m_x and m_z become finite, but their ratio is somewhat arbitrary. This indicates that the system is in a random mixture of Z_2 symmetry-breaking AF (or FM) and $U(1)$ symmetry-breaking XY phases. In other words, the $U(1) \otimes Z_2$ symmetry at $\Delta = -1$ or the SU(2) symmetry at $\Delta = 1$ is broken, and the transitions from the planar-XY order to either FM- or AF-ordered phase is of the first order. Both m_x and m_z become discontinuous at $\Delta = \pm 1$, while m remains continuous across these two high-symmetry lines.

These two first-order phase transition lines can also be identified via other thermal measurements. Figure 6(a) shows the energy per bond u_b as a function of Δ in the

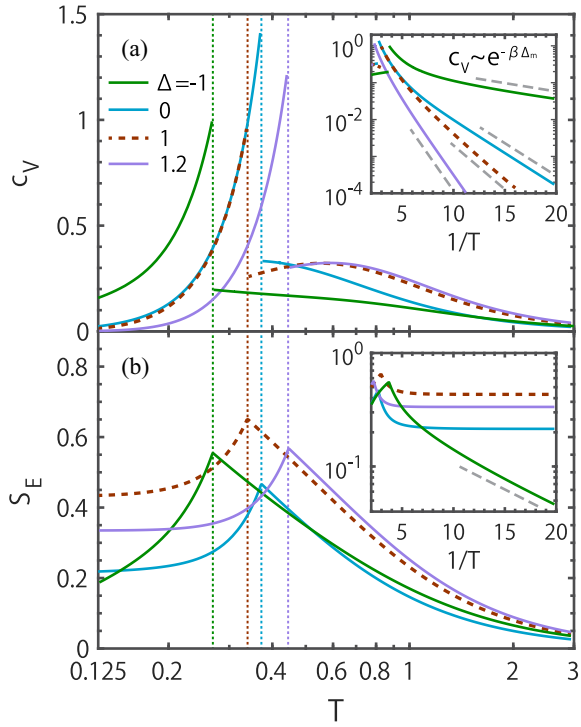

FIG. 4. Temperature dependence of (a) the specific heat c_V and (b) the entanglement entropy S_E for the Heisenberg XXZ model. Logarithmic scale is used for T on the x axis. c_V drops exponentially with T in low temperatures. This exponential decay is emphasized by the dashed gray lines in the inset of (a) where the low temperature part is zoomed in. S_E shows a cusp at T_c and converges to a finite value at low T for $\Delta = 0$, 1, 1.2 [the inset of (b)]. In the FM state, $\Delta \leqslant -1$, S_E drops exponentially to zero in the zero temperature limit, as indicated by the dashed gray line in the inset of (b). The vertical dashed lines in both (a) and (b) represent the critical temperatures of various Δ, with the specific T_c values shown below in Fig. 7.

high-temperature paramagnetic phase with $T = 0.625$, and deep in the symmetry-breaking phase with $T = 0.125$. At $T = 0.125$, the u_b curve shows two turning points at $\Delta = \pm 1$, where the derivative $\partial u_b/\partial\Delta$ becomes discontinuous, as a consequence of the first-order phase transitions. On the other hand, at $T = 0.625$, both u_b and $\partial u_b/\partial\Delta$ vary smoothly, suggesting the absence of phase transitions vs Δ.

Similarly, the phase transitions among these three phases can be seen from the Δ dependence of the entanglement entropy S_E. As shown in Fig. 6(b), S_E exhibits two peaks at $\Delta = \pm 1$ at low temperature $T = 0.125$, which also becomes smooth at a high value $T = 0.625$.

Lastly, the XXZ spin model can be mapped onto a hardcore boson model with nearest-neighboring (NN) interactions, by setting $S_i^- = b_i$ and $S_i^z = b_i^\dagger b_i - 1/2$, where b_i is a hard-core boson operator. In the boson language, the XY phase corresponds to a superfluid phase (SF) with an off-diagonal long-range order, and the FM and AF phases correspond to a Mott insulator (MI) and a charge density wave (CDW) phases, respectively. Along the two vertical phase boundary lines from low temperatures up to T_c, the SF phase coexists with the MI or CDW phases.

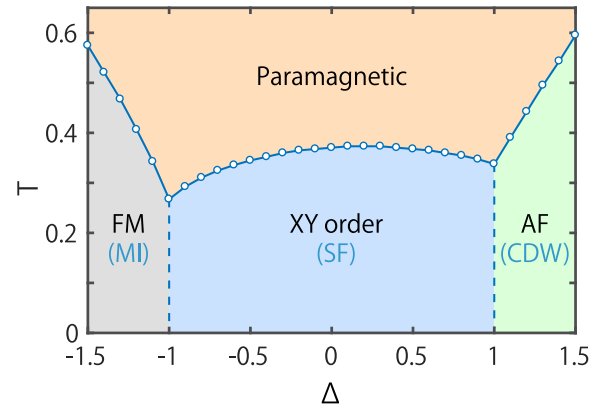

FIG. 5. Δ-T phase diagram of the Bethe-lattice XXZ model, which contains the FM, XY, and AF ordered phases in low temperatures. The solid blue lines (with circle symbols) represent the second-order phase boundaries between the ordered and the paramagnetic phases. In the brackets are corresponding phases in the hardcore boson language, including the SF, CDW, and MI phases (see main text).

B. Low-lying excitations and quasi-Goldstone modes

From the inset of Fig. 4(a), it is clear that the specific heat c_V decays exponentially with β in low temperatures, no matter in which magnetically ordered phase, i.e.,

$$c_V \sim e^{-\beta\Delta_m}. \tag{13}$$

This indicates that there is a finite excitation gap in the low-lying energy spectrum, quantified by the exponent Δ_m in the above equation. The values of Δ_m (Table I) can be obtained by

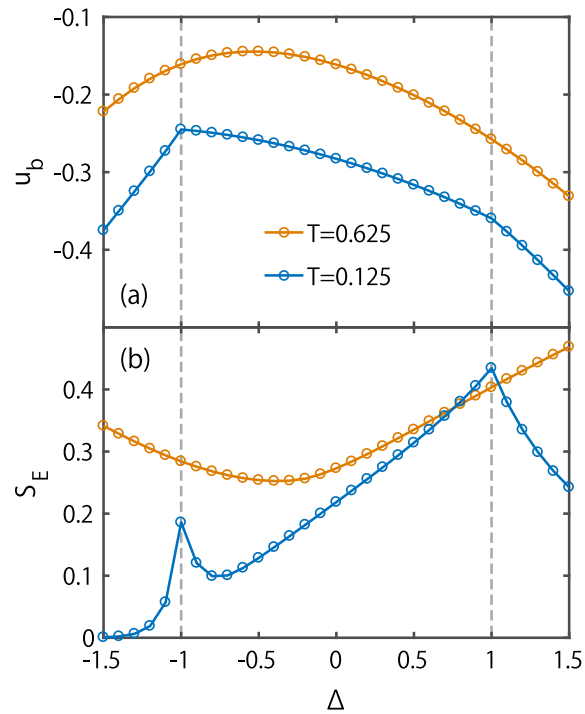

FIG. 6. (a) Internal energy per bond u_b and (b) entanglement entropy S_E vs Δ at two temperatures, $T = 0.125$ and 0.625. The two vertical dashed lines denote the high symmetry points $\Delta = \pm 1$.

TABLE I. Magnon gaps of the XXZ model with different anisotropies Δ and external fields h. The numerical and LSWT results are compared, where the numbers in parentheses in the TTN data are numerical fitting errors.

Model	(Δ, h)	Δ_m (TTN, fitted)	Δ_m (LSWT, $z = 3$)
AF	(1, 0)	0.56(3)	0.5
XY	(0, 0)	0.41(1)	0.3587
FM	(−1, 0)	0.085(3)	0.0858
	(−1, 0.1)	0.186(1)	0.1858
	(−1, 0.2)	0.286(2)	0.2858

fitting the low-T results of the specific heat c_V or the internal energy u. For example, for the FM phase at $\Delta = -1^-$, the low-temperature internal energy is approximately described by the formula

$$u(\beta) - u_0 \simeq g(\beta) e^{-\beta \Delta_m}, \tag{14}$$

where $u_0 = -0.375 - h/2$ is the ground state energy per site, h is an external magnetic field, and $g(\beta)$ is some polynomial prefactor. From the derivative of this equation,

$$\frac{d \ln[u(\beta) - u_0]}{d\beta} = \frac{1}{g}\frac{dg}{d\beta} - \Delta_m,$$

and through a polynomial fitting, the magnon gap Δ_m can be readily read out from the intercept at $T = 1/\beta = 0$. Moreover, for this FM system, one can further tune the magnon gap by changing the external magnetic fields h. The FM excitation gaps of various (small) magnetic fields $h = 0, 0.1, 0.2$ are also obtained by fitting the internal energy curves and shown in Table I, from which we find that $\Delta_m(h) - \Delta_m(0) \simeq h$. This suggests that the elementary excitations in the FM phase are magnons with spin $S = 1$.

To further clarify the nature of low-lying excitations, we have evaluated the correlation length from the transfer matrix along the path $\cdots B \xrightarrow{z} A \xrightarrow{x} B \xrightarrow{z} \cdots$ on the Bethe lattice, meaning going through the z bond of the T_B tensor to T_A, and then through its x bond to the next T_B, and so on. There are also other paths that can be used to define the transfer matrix. But all these paths are physically equivalent and the correlation lengths obtained thereof are also found exactly the same.

Suppose η_0 and η_i are the dominant and the $(i+1)$th largest eigenvalue of the period-two transfer matrix, the correlation length can be determined as

$$\xi_i = 2 \ln^{-1} \left| \frac{\eta_0}{\eta_i} \right|, \tag{15}$$

where ξ_1 is the largest correlation length the system can have, and $\xi_{i>1}$ is related to a shorter-ranged correlation function.

Alternatively, one can also estimate the correlation length ξ directly from the real-space spin-spin correlation function

$$C^\zeta(l) = \langle S_i^\zeta S_{i+l}^\zeta \rangle - \langle S_i^\zeta \rangle \langle S_{i+l}^\zeta \rangle \quad (\zeta = x, y, z), \tag{16}$$

where l measures the distance between the two sites along the path. Given the $C^\zeta(l)$ data, the correlation length ξ can be obtained by fitting the large-distance correlation function with an exponentially varying function.

Figures 7(a)–7(d) show the correlation lengths obtained with the above two approaches. The correlation length $\xi^{z(x)}$

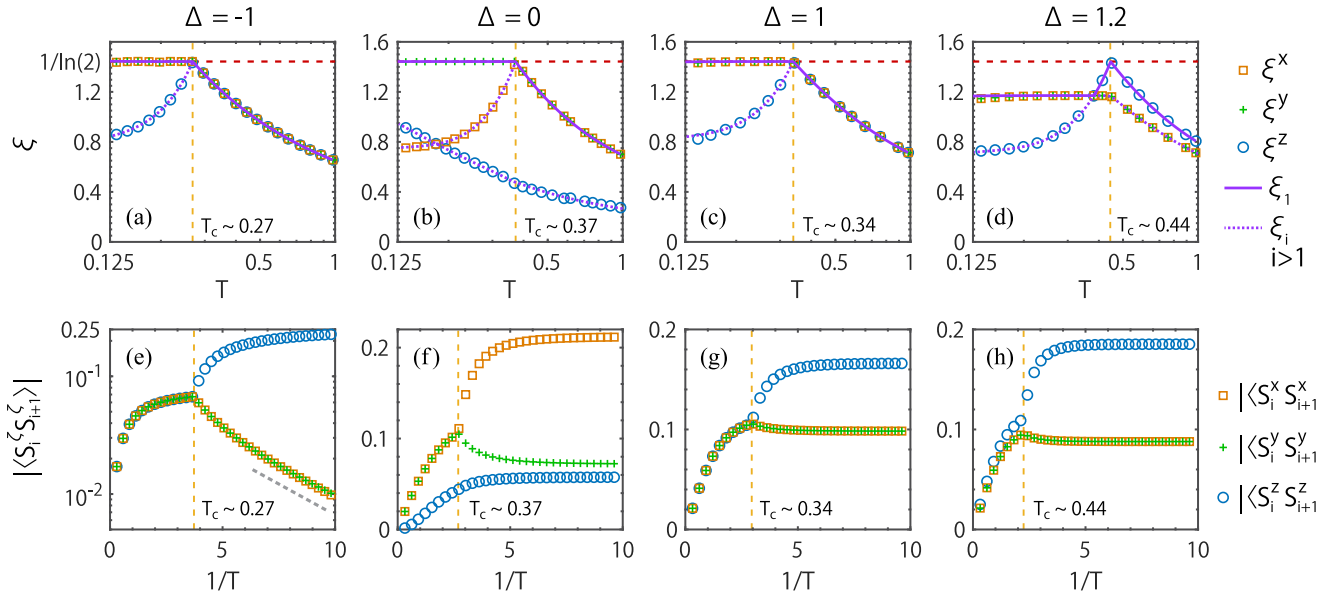

FIG. 7. (a)–(d) Correlation length ξ vs T and (e)–(h) the absolute value of corresponding NN correlations $|\langle S_i^\zeta S_{i+1}^\zeta \rangle|$ $(\zeta = x, y, z)$ vs $1/T$, for $\Delta = -1$, 0, 1, and 1.2, respectively. In (a)–(d), the x axis is in logarithmic scale. The purple lines $\{\xi_i\}$ are extracted from the transfer-matrix spectra, in which the solid lines are the leading correlation length ξ_1 and the dashed ones are certain shorter correlation length ξ_i [see Eq. (15) for definition, $i > 1$]. And the markers label the correlation lengths $\xi^{x,y,z}$ fitted from the spin-spin correlators $C^{x,y,z}(l)$. The dashed gray line in (e) illustrates the exponential decay vs $1/T$, as a guide to the eye. For $\Delta = \pm 1$ in (a), (c), (e), and (g), we have chosen the z axis as where the spontaneous magnetization takes place and $\xi^{x,y}$ are related to transverse fluctuating modes on the XY plane. The vertical dashed (yellow) lines in all panels represent the critical temperatures T_c determined in Fig. 4, and the horizontal dashed (red) lines in (a)–(d) denote the maximal correlation length $\xi_c = 1/\ln(2)$.

determined from the dominating correlators, $C^z(l)$ for $\Delta = \pm 1, 1.2$ and $C^x(l)$ for $\Delta = 0$, exhibits cusps exactly at the critical temperatures T_c. The value of the correlation length at the critical point, $\xi_c = 1/\ln(2) \simeq 1.4427$, equals the critical upper bound of the correlation length on the $z = 3$ Bethe lattice. As discussed in Ref. [10], the number of spins that correlate with a root spin at a given site grows exponentially with their distances. Therefore, a magnetic order-disorder phase transition with a diverging magnetic susceptibility happens when ξ, though being finite, reaches the critical value $1/\ln(z-1)$.

For the cases $\Delta = \pm 1$ shown in Figs. 7(a) and 7(c), the correlation lengths, $\xi^{x,y,z}$ along all three directions, are all equal to the dominant correlation length ξ_1 in the paramagnetic phase above T_c. Below T_c, the transverse excitation modes remain critical and do not change with temperature, i.e., the corresponding correlation lengths still equal the dominant one $\xi^{x,y} = \xi_1 = \xi_c$. Moreover, the longitudinal ξ^z drops immediately below T_c with decreasing temperature, due to the formation of magnetic order along the z direction. Similar critical behavior has been observed in Fig. 7(b) with $\Delta = 0$, where the degeneracy between ξ^x and ξ^y is broken, since the ordering of spins happens along the x direction.

For the case $|\Delta| > 1$ in Fig. 7(d), $\xi^z = \xi_1$ is still the dominant correlation length above T_c, which reaches the critical value ξ_c and drops below T_c. On the other hand, $\xi^{x,y}$ never reaches the critical value $1/\ln 2$, although they do not decay below T_c, and surpasses ξ^z at a temperature below T_c.

The peculiar behaviors of the transverse correlation lengths observed in the ordered phases are quite remarkable. It indicates that although the true Goldstone modes are absent in the continuous symmetry-breaking phases [44], the transverse excitations remain "critical" with a maximal correlation length $\xi_c = 1/\ln(2)$ on the Bethe lattice. These quasicritical transverse excitation modes are reminiscent of the Goldstone modes in a truly gapless continuous symmetry-breaking system, and they can be regarded as somewhat "renormalized" Goldstone modes.

Distinct from the true gapless modes, and as the finite correlation lengths imply, these quasi-Goldstone modes are always gapped, and they become activated only above certain finite energy scales/temperatures, giving rise to the finite-T phase transitions. Note that such kind of quasi-Goldstone modes are absent in the Z_2 symmetry-breaking phase, again similar to the two-dimensional lattices where Goldstone modes are absent for $|\Delta| > 1$.

As a complementary to correlation length data, we show in Figs. 7(e)–7(h) the absolute value of NN correlators $|\langle S_i^\zeta S_{i+1}^\zeta \rangle|$ ($\zeta = x, y, z$). In Figs. 7(e) and 7(g) we see distinct behaviors of NN correlators between the FM ($\Delta = -1$) and AF ($\Delta = 1$) cases. In the AF phase, $|\langle S_i^{x(y)} S_{i+1}^{x(y)} \rangle|$ approaches a finite value in the zero temperature limit. However, in the FM case, $|\langle S_i^{x(y)} S_{i+1}^{x(y)} \rangle|$ decays exponentially as T decreases and it approaches zero in the $T = 0$ limit. This is consistent with the fact that the FM ground state is simply a direct-product state $|\uparrow, \uparrow, \ldots, \uparrow\rangle$, while the AF ground state bears quantum entanglement. Moreover, as shown in Figs. 7(f) and 7(h), $|\langle S_i^x S_{i+1}^x \rangle|$ and $|\langle S_i^z S_{i+1}^z \rangle|$ are strongest NN correlators in the $\Delta = 0$ and 1.2 cases, respectively. In addition, other spin correlators in these two cases converge to finite values in the $T = 0$ limit.

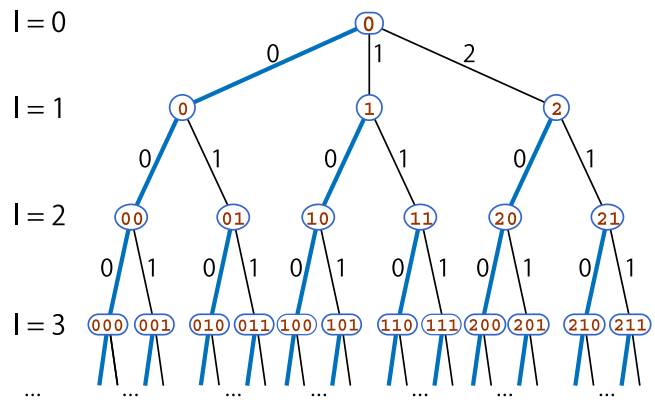

FIG. 8. Site labelings on the $z = 3$ Bethe lattice, in both the real space r and its dual q coordination. l indicates the layers, and "0", "1", and "2" on the links label different branches, the combination of which uniquely determines a path which can be further used to mark the sites. Thick blue lines indicate the effective 1D paths along which magnons propagate in the q space.

IV. LINEAR SPIN WAVE THEORY

Here we provide a LSWT analysis of the XXZ model on the Bethe lattice. The results reveal more information on the low-lying excitations, especially on the quasi-Goldstone mode in the continuous symmetry-breaking phase.

A. The ferromagnetic Heisenberg model

We first consider the excitations in the FM phase with $\Delta < -1$. By taking a $U(1)$ rotation $\exp(i\pi S_n^z)$ for all the spins on the B sublattice, we can transform Eq. (1) into the form

$$H = \sum_{\langle i,j \rangle} (-S_i^x S_j^x - S_i^y S_j^y + \Delta S_i^z S_j^z) - h \sum_i S_i^z. \tag{17}$$

To carry out the linear spin-wave expansion, we choose an arbitrary site as a "root," labeled as $R_0 = 0$, and then there exists a unique path that connects it to any other lattice site, rendering a convenient way to label the Bethe lattice sites. More specifically, we label the lattice according to the rule shown in Fig. 8: a site in the lth layer from the root is represented by l indices $R_l = (r_1 r_2, \ldots, r_l)$, where $r_\lambda = 0, 1, \ldots, \tilde{z} - 1$ ($\lambda = 1, 2, \ldots, l$) denotes the way a path can choose at the $(\lambda - 1)$th branching point. On a z-coordinated Bethe lattice, $\tilde{z} = z$ for the $l = 1$ layer and $\tilde{z} = z - 1$ for the rest layers.

Assuming all spins are up polarized in the ground state, we exploit the Holstein-Primakoff (HP) transformation and take the leading approximation for the spin operators $S^+ = \sqrt{2S}a$, $S^- = \sqrt{2S}a^\dagger$, and $S^z = S - a^\dagger a$, where $a, a^\dagger$ are boson annihilation and creation operators, respectively. Under the linear spin-wave approximation, the Hamiltonian becomes

$$H = (-zS\Delta + h) \sum_{l,R_l} n_{R_l} - S \sum_{l,R_l} \sum_{r_{l+1}} \left(a_{R_l}^\dagger a_{R_l r_{l+1}} + \text{H.c.} \right), \tag{18}$$

where $n_{R_l} = a^\dagger_{R_l} a_{R_l}$ is the particle number operator, and a constant energy term is dropped for the sake of simplicity.

To diagonalize the Hamiltonian (18), we first take the following multidimensional discrete Fourier transformation:

$$a_{Q_l} = \sum_{R_l} \left(\prod_{\lambda=1}^{l} U_{q_\lambda, r_\lambda} \right) a_{R_l}, \tag{19}$$

where $Q_l = (q_1 q_2 \cdots q_l)$ are the "quasimomenta" which are dual to R_l, and U is a unitary matrix

$$U_{q_\lambda, r_\lambda} = \frac{1}{\sqrt{\tilde{z}}} e^{2\pi i q_\lambda r_\lambda / \tilde{z}}. \tag{20}$$

Through this transformation we generate a Bethe lattice with exactly the same geometry in the q space, i.e., $q_l \in \{0, 1, \ldots, \tilde{z} - 1\}$.

Under the above transformation, the hopping term in Eq. (18) becomes

$$\sum_{R_l, r_{l+1}} a^\dagger_{R_l} a_{R_l r_{l+1}} = \sqrt{\tilde{z}} \sum_{Q_l} a^\dagger_{Q_l} a_{Q_l, 0}, \tag{21}$$

where $(Q_l, 0)$ denotes a site on the $(l+1)$th shell, next to site Q_l and with $q_{l+1} = 0$. On the other hand, the occupation number term remains as a number operator in the q space

$$\sum_{R_l} a^\dagger_{R_l} a_{R_l} = \sum_{Q_l} a^\dagger_{Q_l} a_{Q_l}. \tag{22}$$

More details of the transformation can be found in Appendix C.

Equation (21) with its Hermitian conjugate implies that a boson on the site Q_l can only hop to site $(Q_l, 0)$, and vice versa. $(Q_l, 0)$ indicate a site on $(l+1)$th shell, which is on the same branch of Q_l and further has $q_{l+1} = 0$. Therefore, for any given site Q_l with $q_l \neq 0$, there exists a one-dimensional path, consisting of Q_l, $(Q_l, 0)$, $(Q_l, 0, 0)$,..., etc.

The Hamiltonian on this half-infinite one-dimensional chain is tridiagonal, i.e.,

$$H_{\mathrm{FM}} = \sum_{i=0}^{\infty} (-zS\Delta + h) b_i^\dagger b_i - S\sqrt{\tilde{z}} (b_i^\dagger b_{i+1} + \mathrm{H.c.}), \tag{23}$$

where $b_i = a_{Q_l \underbrace{00\cdots0}_{i}}$, and $b_0 = a_{Q_l}$ is the starting node from which the one-dimensional path, depicted by a thick line in Fig. 8, is defined.

Second, we solve the above chain Hamiltonian via a conventional Fourier transformation, and the spin wave energy spectrum is found to be

$$\varepsilon(\kappa) = -zS\Delta + h - 2S\sqrt{z-1}\cos\kappa, \tag{24}$$

where $\kappa \in [0, \pi]$ is the momentum along the "effective" chains on the q-space Bethe lattice. From Eq. (24), as well as the plot in Fig. 9, we find the magnon excitation energy gap as

$$\Delta_m = -zS\Delta + h - 2S\sqrt{z-1}. \tag{25}$$

The single magnon state is an eigenstate of the original Heisenberg FM model, and thus the magnon gap Δ_m obtained in Eq. (25) constitutes an upper bound of the true excitation gap of the system. As a matter of fact, as shown in Table I, the energy gap obtained with this equation, $\Delta_m = 3/2 - \sqrt{2} \simeq 0.0858$, is very close to the value estimated from the TTN calculation. In addition, from Eq. (25) one can see clearly that Δ_m increases linearly with h, in excellent consistency with the TTN results (see also Table I).

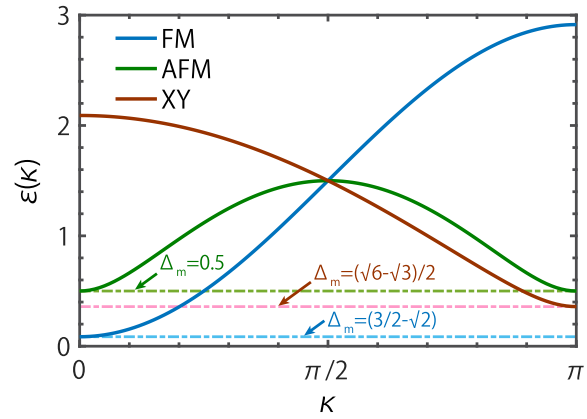

FIG. 9. Magnon bands of the FM, AF, and XY Heisenberg models on the $z = 3$ Bethe lattice, where the horizontal dashed lines indicate the magnon gap values Δ_m.

From the above discussion we notice that each branch of magnon excitations is confined to a one-dimensional path which is formed by a symmetrized ($q = 0$) superposition of $\tilde{z}$ real-space sites. This symmetry has already been exploited in some previous works [5,20,45,46], however, the r-q transformation we introduce here works in a more generic way.

B. Antiferromagnetic Heisenberg model

For the AF model with $\Delta \geqslant 1$, the linear spin wave expansion can be similarly done by explicitly considering the spin orientations on the two sublattices. We start from the configuration that all the spins are upward aligned on the A sublattice and downward aligned on the B sublattice. Accordingly, we take a two-sublattice HP transformation, i.e., $S_i^+ = \sqrt{2S} a_i$, $S_i^- = \sqrt{2S} a_i^\dagger$, and $S_i^z = S - a_i^\dagger a_i$, for $i \in A$, and $S_j^+ = \sqrt{2S} a_j^\dagger$, $S_j^- = \sqrt{2S} a_j$, and $S_j^z = a_j^\dagger a_j - S$ for $j \in B$. Therefore, the Hamiltonian under the linear spin wave approximation can be written as

$$H = zS\Delta \sum_{l, R_l} n_{R_l} + S \sum_{l, R_l} \sum_{r_{l+1}} \left(a_{R_l} a_{R_l r_{l+1}} + a^\dagger_{R_l} a^\dagger_{R_l r_{l+1}} \right). \tag{26}$$

A constant term is again omitted in obtaining the above expression.

To cope with the two-sublattice structure, we need to adopt different transformations on different sublattices, namely taking $\tilde{U}_{q,r} = U_{q,r}$ on the A sublattice and $\tilde{U}_{q,r} = U^\dagger_{q,r}$ on the B sublattice. Under this transformation, the pair annihilation term becomes (Appendix C)

$$\sum_{R_l, r_{l+1}} a_{R_l} a_{R_l r_{l+1}} = \sqrt{\tilde{z}} \sum_{Q_l} a_{Q_l} a_{Q_l, 0}. \tag{27}$$

The above Hamiltonian can then be effectively represented as a direct sum of the infinite-many one-dimensional models

defined by the model

$$H_{\mathrm{AF}} = \sum_{i=0}^{\infty} S[z\Delta\, b_i^\dagger b_i + \sqrt{\tilde{z}}(b_i b_{i+1} + b_i^\dagger b_{i+1}^\dagger)]. \tag{28}$$

Employing the standard Bogoliubov transformation, the energy spectrum of H_{AFC} is found to be (and plotted in Fig. 9)

$$\varepsilon(\kappa) = S\sqrt{(z\Delta)^2 - 4(z-1)\cos^2\kappa}, \quad \kappa \in [0, \pi]. \tag{29}$$

The energy gap is $\Delta_m = S(z-2)$, for $z \geqslant 3$. Since the single-magnon excitation state is not an eigenstate of the original AF model, Δ_m may not be an upper bound of the true excitation gap. Nonetheless, from Table I we observe that Δ_m still provides a quite good estimate of the magnon gap.

C. The XY model

The magnon bands of FM and AF cases become unstable when $|\Delta| < 1$ (more precisely, when $|\Delta| < 2\sqrt{z-1}/z$). To perform a linear spin-wave analysis for the XY phase, we needs to start from a classical state in which the spins are ordered on the XY plane.

Below, for the sake of simplicity, we consider only the case $\Delta = 0$. The Hamiltonian can be equivalently written as

$$H = \sum_{\langle i,j\rangle} S_i^z S_j^z + S_i^x S_j^x. \tag{30}$$

Under the linear spin-wave approximation, it becomes

$$H = zS\sum_{l,R_l} n_{R_l} + \frac{S}{2}\sum_{l,R_l}\sum_{r_{l+1}} \left(a_{R_l} + a_{R_l}^\dagger\right)\left(a_{R_l r_{l+1}} + a_{R_l r_{l+1}}^\dagger\right). \tag{31}$$

To solve this problem, we use the following r-q transformation matrix

$$U_{q,r} = \begin{cases} 1/\sqrt{\tilde{z}}, & q = 0, \\ \sqrt{\frac{2}{\tilde{z}}}\cos\left[\frac{\pi}{\tilde{z}}\left(r+\frac{1}{2}\right)q\right], & q = 1, 2, \ldots, \tilde{z}-1. \end{cases} \tag{32}$$

This particular choice ensures $U_{q,r}$ to be a real orthogonal matrix with the property

$$\sum_r U_{q,r} = \sqrt{\tilde{z}}\delta_{q,0}.$$

From this, again we obtain an effective one-dimensional boson model

$$H_{\mathrm{XY}} = \sum_{i=0}^{\infty} S\left[z b_i^\dagger b_i + \frac{\sqrt{\tilde{z}}}{2}(b_i + b_i^\dagger)(b_{i+1} + b_{i+1}^\dagger)\right]. \tag{33}$$

Diagonalizing this Hamiltonian using the Bogoliubov transformation (Appendix D), the magnon excitation energy is found to be (Fig. 9)

$$\varepsilon(\kappa) = S\sqrt{z(z + 2\sqrt{z-1}\cos\kappa)}, \quad \kappa \in [0, \pi]. \tag{34}$$

The excitation gap is $\Delta_m = S\sqrt{z}(\sqrt{z-1} - 1)$, which is $(\sqrt{6} - \sqrt{3})/2 \approx 0.3587$ for $S = 1/2$ and $z = 3$, close to the numerical results, 0.41(1), shown in Table I.

V. SUMMARY

We have investigated the Heisenberg XXZ model using both the canonical TTN and LSWT on the $z = 3$ Bethe lattice. Through efficient and accurate tensor network simulations, we have obtained the finite-temperature phase diagram of the model. The system undergoes a second-order phase transition at finite temperature, and three kinds of magnetic ordered phases are uncovered in low T. The correlation lengths, as well as bipartite entanglements, though exhibiting their maximal values at the transition temperature T_c, are found to be always finite on the Bethe lattice. Correspondingly, the low-lying excitations are revealed, through both numerical TTN and analytical spin wave calculations, to be gapped, even in the parameter range where the system breaks spontaneously the continuous symmetries.

Therefore, although the conventional gapless Goldstone modes are absent, quasi-Goldstone transverse fluctuation modes have been observed in the Bethe lattice XXZ model. When the system spontaneously breaks the continuous symmetries, the transverse correlation lengths reach the critical value $\xi_c = 1/\ln(z-1)$, and remain there for $T \leqslant T_c$. Here ξ_c is the maximal correlation length that is allowed on the Bethe lattice.

The results obtained on the Bethe-like lattices can be used to understand physical properties of quantum lattice models on the honeycomb, square, or other regular lattices. In addition, the canonical TTN method we proposed works very generally, and it can be applied to other fundamental quantum many-body models, such as the frustrated Heisenberg and Hubbard models defined on the Bethe-like lattices, etc.

ACKNOWLEDGMENTS

This work was supported by the National Natural Science Foundation of China (11974036, 11834014, 11888101), the National R&D Program of China (2017YFA0302900). W.L. is indebted to Andreas Weichselbaum for helpful discussions. D.-W.Q. and W.L. would like to thank Jan von Delft for hospitality during a visit to LMU Munich, where part of this work was performed.

APPENDIX A: TENSOR UPDATE ON THE BETHE LATTICE

1. Bethe lattice update

An imaginary time evolution can be employed to cool down the TTN density operator on the Bethe lattice, where the local tensors are updated via a simple scheme. The details are illustrated in Fig. 10 and elaborated below. We take the the x-bond update as an example, and the successive projection procedures on the other two, i.e., y and z bonds, can be accomplished similarly. The three projection substeps on different bonds constitute a full Trotter step of small imaginary-time slice τ.

(a) Absorb the environment matrices λ_y and λ_z to the T tensors and construct the W tensor [Fig. 10(a)]

$$(W_\alpha)_{xyz}^{\sigma_\alpha\sigma'_\alpha} = (T_\alpha)_{xyz}^{\sigma_\alpha\sigma'_\alpha}\lambda_y\lambda_z, \tag{A1}$$

where $\alpha = A, B$.

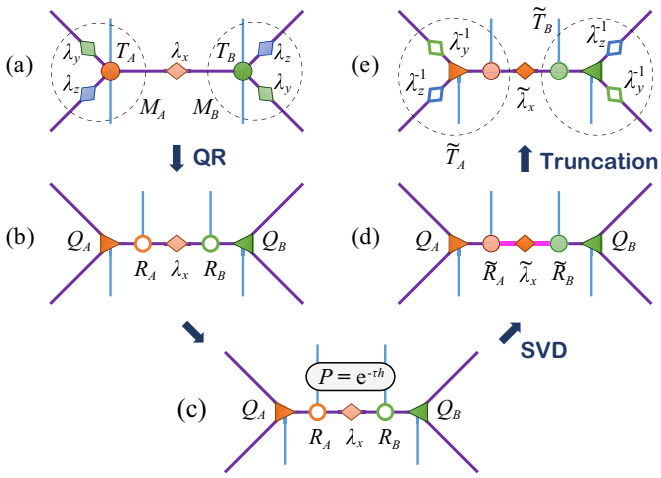

FIG. 10. A single step of imaginary-time evolution on an x bond, see Appendix A 1 for details.

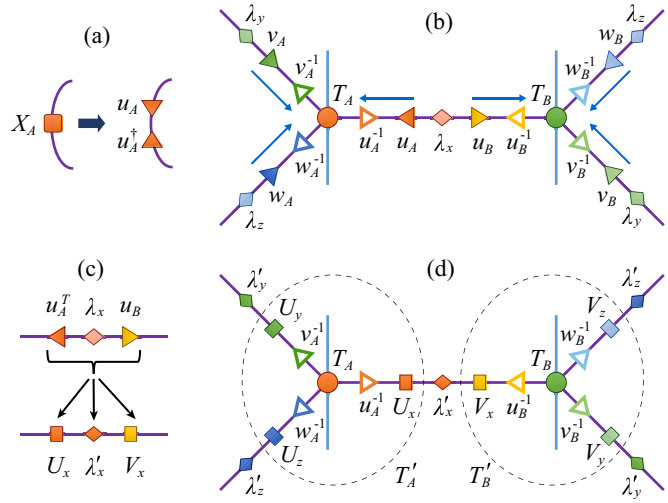

FIG. 11. Canonicalization procedure of the TTN, where the x-bond procedure is taken as an example in (a) and (c). See Appendix A 2 for details.

(b) Perform a QR decomposition of W_α [Fig. 10(b)]

$$(W_\alpha)^{\sigma_\alpha \sigma'_\alpha}_{xyz} = \sum_{x'} (Q_\alpha)^{\sigma'_\alpha}_{x'yz} (R_\alpha)^{\sigma_\alpha}_{x'x}, \tag{A2}$$

which splits off the upper physical indices σ_α into the R tensors.

(c) Construct a base tensor B by combining λ_x with the two adjacent tensors R_A and R_B

$$B^{\sigma_A \sigma_B}_{x'_A x'_B} = \sum_{x} (R_A)^{\sigma_A}_{x'_A x} \lambda_x (R_B)^{\sigma_B}_{x'_B x}, \tag{A3}$$

and apply the two-site imaginary-time evolution gate $P = e^{-\tau h_x}$ onto the base tensor [Fig. 10(c)]

$$\tilde{B}^{\sigma_A \sigma_B}_{x'_A x'_B} = \sum_{\sigma'_A, \sigma'_B} P^{\sigma_A \sigma_B}_{\sigma'_A \sigma'_B} B^{\sigma'_A \sigma'_B}_{x'_A x'_B}. \tag{A4}$$

(d) Reshape $\tilde{B}$ into a matrix by grouping together σ_A with x'_A as a single index, and σ_B with x'_B into another. Then we perform a matrix SVD

$$(\tilde{B})^{\sigma_A \sigma_B}_{x'_A x'_B} = \sum_{x} (\tilde{R}_A)^{\sigma_A}_{x'_A x} \tilde{\lambda}_x (\tilde{R}_B)^{\sigma_B}_{x'_B x}, \tag{A5}$$

as shown in Fig. 10(d). Note that the matrix dimension of $\tilde{\lambda}_x$ is enlarged by d^2 times after the bond evolution, which needs to be truncated by retaining only the largest D singular values and corresponding bond bases. After this proper truncation of bond states, we update the tensors $\tilde{R}_a$, $\tilde{R}_b$, and $\tilde{\lambda}_x$ accordingly.

(e) Combine $\tilde{R}$ to the corresponding Q tensors, and spit off the $\lambda_{y(z)}$ matrices, that have been absorbed into Q in steps (a) and (b), by multiplying their inverse matrices $\lambda^{-1}_{y(z)}$ to Q. Thus we obtain the updated $\tilde{T}$ tensors [Fig. 10(e)]

$$(\tilde{T}_\alpha)^{\sigma_\alpha \sigma'_\alpha}_{xyz} = \sum_{x'} \lambda_y^{-1} \lambda_z^{-1} (Q_\alpha)^{\sigma'_\alpha}_{x'yz} (\tilde{R}_\alpha)^{\sigma_\alpha}_{x'x}, \tag{A6}$$

where again $\alpha = A, B$ denoting two sublattices.

In the ground state optimization [10], the above procedure suffices to produce accurate results. The truncation errors do not accumulate, and τ can be tuned to a sufficiently small value, say $\tau \sim 10^{-4}$ in the end of projections. However, in the finite-temperature simulations, now the truncation errors accumulate, we therefore need to carefully optimize the truncations in every single step to improve the overall performance. Note that $e^{-\tau h^i_\zeta}$ ($\zeta = x, y, z$) is not unitary and breaks the orthogonality of bond basis, and thus TTN deviates the canonical form after each step of imaginary-time evolution. Therefore, a canonicalization procedure of the TTN is needed to restore the orthogonality of bond bases and optimize the truncations.

2. Canonicalization procedure of TTN

Following a similar line of standard procedure developed in the matrix product [9,25,26] as well as tensor product states [29], we present below the canonicalization of TTN on the Bethe lattice.

(i) As shown in Fig. 11(a), we decompose the dominant eigenvectors of the transfer tensors as

$$\begin{aligned} (X_\alpha)_{x,x'} &= \sum_{x''} (u_\alpha)_{x,x''} (u^\dagger_\alpha)_{x'',x'}, \\ (Y_\alpha)_{y,y'} &= \sum_{y''} (v_\alpha)_{y,y''} (v^\dagger_\alpha)_{y'',y'}, \\ (Z_\alpha)_{z,z'} &= \sum_{z''} (w_\alpha)_{z,z''} (w^\dagger_\alpha)_{z'',z'}, \end{aligned} \tag{A7}$$

where $\alpha = A, B$. Since in practice X_α, Y_α, and Z_α matrices are symmetric, the decomposition can be done via the eigenvalue or the Cholesky decomposition.

(ii) Insert pairs of reciprocal matrices, $u_\alpha u_\alpha^{-1}$, $v_\alpha v_\alpha^{-1}$, and $w_\alpha w_\alpha^{-1}$, to the three geometrical bonds, as shown in Fig. 11(b). Order of the matrix multiplication has also been specified by the arrows, e.g., we contract the first index of u_A with λ_x and the second index of u_A^{-1} with T_A.

(iii) Now we perform the bond update by combining the bond matrices and then perform a SVD. As shown in Fig. 11(c), we take the x bond as an example, i.e.,

$$u_A^T \lambda_x u_B = U_x \lambda'_x V_x. \tag{A8}$$

U_x and V_x are unitary matrices, and λ_x' is used to update the bond diagonal matrix.

(iv) As shown in Fig. 11(d), we absorb u^{-1}, v^{-1}, and w^{-1} matrices, as well as the adjacent unitary matrices U and V, into the T_α tensors, and update T_A' and T_B'.

After the above procedure on the x bond (and simultaneously on the y and z bonds), the updated tensors T_α' satisfy the canonical conditions [see Eq. (2) of the main text], and the dominating eigenvectors $X_\alpha, Y_\alpha, Z_\alpha$ are now gauged into identities.

3. Simple vs canonical schemes

Now we provide some numerical benchmarks of the simple and canonical update schemes, showing the advantage of the latter in both the accuracy and robustness. Here by canonical scheme we mean the combined procedure using techniques introduced in both Appendixes A 1 and A 2; while by simple scheme we mean a poor man's approach where the canonicalization operations in Appendix A 2 are skipped.

We consider the Heisenberg model ($\Delta = 1$), and compare the entanglement entropy S_E and the number of iterations N_{iter} required to reach a convergence in determining the dominant eigenvectors in Eq. (8) of the main text. Although the entanglement entropy S_E defined in Eq. (11) is rigorously defined only for canonical TTN, we can nevertheless take "S_E" from the simple scheme as a measurement of entanglement for comparisons.

As seen in Fig. 12(a), the two S_E curves almost coincide for $T > T_c$. However, their behaviors start to differ at the critical temperature T_c. The curve of the canonical scheme shows a cusp at the critical temperature and slowly converges to a smaller zero-temperature entanglement value, while that of the simple scheme still rises smoothly until collapsing at certain lower temperature below T_c. After this "jump," the simple scheme curve lies almost on top of the canonical curve, and both converge to the $T = 0$ entanglement value in nearly the same rate.

Correspondingly, as shown in Fig. 12(b), N_{iter} peaks at T_c in the canonical scheme, and it peaks both at T_c and the jump point at a lower T in the simple scheme curve. The second peak in N_{iter} in the simple scheme belongs to an numerical "artifact," since no phase transition really takes place there.

Apart from the artifact in S_E, the more severely accumulated errors in the simple scheme, as the temperature lows down, may cause other problems. In practice, sometimes the simple scheme is found to generate "wrong" metastable thermodynamic results, e.g., magnetic moments, at low temperatures $T < T_c$.

To conclude, the canonical scheme turns out to be more accurate and robust, and it is thus mostly adopted in our practical simulations.

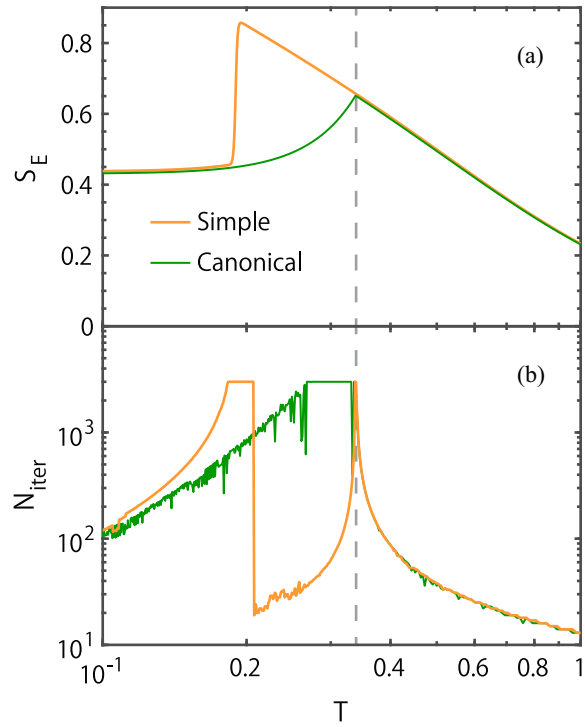

FIG. 12. Comparisons between the simple and canonical update optimization schemes on (a) the entanglement entropy S_E and (b) iteration number N_{iter} for $\Delta = 1$. The x axis is in logarithmic scale. The dashed gray line denotes the critical point T_c for $\Delta = 1$, and the convergence tolerant for the iterations is 10^{-7}, with the maximal iteration number restricted up to 3000 in practice.

APPENDIX B: CLASSICAL ISING MODEL ON THE BETHE LATTICE

In this Appendix we provide the rigorous solution of the classical Ising model on the Bethe lattice via transfer tensor techniques. The TTN algorithms introduced in Sec. II can also be employed to compute this classical model, and the comparisons between the numerical and rigorous results thus provide a first benchmark of the TTN algorithm.

The Hamiltonian (energy) of the classical Ising model reads $H = -J\sum_{\langle i,j\rangle}\sigma_i\sigma_j$, where $J = 1$ is the energy scale, $\langle i, j\rangle$ means NN sites on the Bethe lattice, and $\sigma = \pm 1$ denotes the classical Ising variables.

This Ising model can be solved exactly through a number of essentially equivalent methods, including the self-similarity [3,47], cavity approaches [3,48], etc. By solving the generalized eigenvalue problem, we find the dominant eigenvectors of the transfer tensor $\mathcal{T}$, from which we further obtain the exact expression of thermal quantities.

First, we rewrite the partition function as a TTN, i.e.,

$$\mathcal{Z} = \sum_{\{\sigma\}} e^{\beta\sigma_1\sigma_2}\mathcal{T}^{\sigma_{11}\sigma_{12}}_{\sigma_1}\mathcal{T}^{\sigma_{21}\sigma_{22}}_{\sigma_2}\mathcal{T}^{\sigma_{111}\sigma_{112}}_{\sigma_{11}}\mathcal{T}^{\sigma_{121}\sigma_{122}}_{\sigma_{12}}\cdots, \tag{B1}$$

where $\mathcal{T}$ is a transfer tensor, and $\sigma_{1(2)}$ sits in the two central sites in the bond-centered Bethe lattice, see, e.g., Fig. 1(b). The $r_1 r_2 \cdots r_l$ labeling in $\sigma_{r_1 r_2 \cdots r_l}$ follows the convention shown in Fig. 8, but r_i starts from 1 instead of 0 here.

Efficient contractions of this infinite TTN can be implemented by finding the dominant (generalized) eigenvectors V_σ of the transfer tensor $\mathcal{T}^{\sigma_1\sigma_2}_{\sigma_0} = e^{\beta\sigma_0(\sigma_1+\sigma_2)}$, i.e.,

$$\sum_{\sigma_1,\sigma_2}\mathcal{T}^{\sigma_1\sigma_2}_{\sigma_0}V_{\sigma_1}V_{\sigma_2} = \eta V_{\sigma_0}, \tag{B2}$$

with the (generalized) eigenvalue η. By writing it down explicitly, we have

$$\begin{aligned} V_+^2 e^{2\beta} + V_-^2 e^{-2\beta} + 2V_+V_- &= \eta V_+, \\ V_+^2 e^{-2\beta} + V_-^2 e^{2\beta} + 2V_+V_- &= \eta V_-. \end{aligned} \tag{B3}$$

Since Eq. (B3) does not constitute a linear system of equations, one has a gauge degree of freedom in determining the eigenvalue η as well as the eigenvector $V_\pm$. Nevertheless, we can eliminate η from the equations, and arrive at a cubic equation after some rearrangement,

$$(x-1)[x^2 + (1-e^{2\beta})x + 1] = 0, \tag{B4}$$

where $x = \sqrt{V_+/V_-}$. Note that the eigenvalue can now be expressed as $\eta = V_+(x/e^\beta + e^\beta/x)^2$, which cannot be uniquely determined and depends on the normalization condition of V_σ (see related discussions in Sec. II C).

The (unnormalized) probability distribution for two neighboring spin variables is $\rho_{\sigma_1\sigma_2} = e^{\beta\sigma_1\sigma_2} V_{\sigma_1} V_{\sigma_2}$. By summing over σ_2, we can get the distribution of a single spin σ_1, from which the magnetization can be derived as $\langle\sigma\rangle = \sum_{\sigma_1}\sigma_1\rho_{\sigma_1}/\sum_{\sigma_1}\rho_{\sigma_1} = (x^3-1)/(x^3+1)$. Note that x is just the root of Eq. (B4), and thus the local magnetization can be uniquely determined.

The order parameter, i.e., the spontaneous magnetization m, reads

$$m = \langle\sigma_1\rangle_\beta = \begin{cases} 0, & \beta \leqslant \beta_c, \\ \pm\frac{\omega}{\omega-2}\sqrt{\frac{\omega-3}{\omega+1}}, & \beta > \beta_c, \end{cases} \tag{B5}$$

with $\omega = e^{2\beta}$ and the critical point $\beta_c = 1/T_c = \ln(3)/2 \simeq 0.5493$.

Apparently the root $x = 1$ (and thus $m = 0$) corresponds to the paramagnetic solution, while the two roots of the remaining quadratic equation in Eq. (B4) reflects the twofold degenerate FM states. The $\pm$ sign represents the spin-up and spin-down solutions, respectively, given that the discriminant $(1-e^{2\beta})^2 - 4 > 0$, i.e., $\beta > \beta_c = \ln(3)/2$.

The internal energy per bond u_b can be determined from $\rho_{\sigma_1\sigma_2}$, which is

$$u_b = -\langle\sigma_1\sigma_2\rangle_\beta = \begin{cases} \frac{1-\omega}{1+\omega}, & \beta \leqslant \beta_c, \\ \frac{4}{(\omega^2-1)(\omega-2)} - 1. & \beta > \beta_c. \end{cases} \tag{B6}$$

It is clear that the u_b curve exhibits a singular point at the transition temperature β_c.

On the other hand, the Bethe-lattice Ising model can also be solved by the TTN techniques. By performing a decomposition following Eq. (3), and then an imaginary-time evolution procedure, we obtain the thermal density matrix $\rho(\beta) = e^{\beta\sum_{\langle i,j\rangle}\sigma_i\sigma_j}$ of the classical Ising model on the Bethe lattice. On top of that, we can further calculate the thermal quantities, including the magnetization, energy, specific heat, etc.

In Fig. 13 we compare the TTN results of the spontaneous magnetization and the specific heat to the exact solution, where excellent agreements can be observed. This can be ascribed to the absence of Trotter errors in the calculations, and also to no essential truncations in the procedure of cooling.

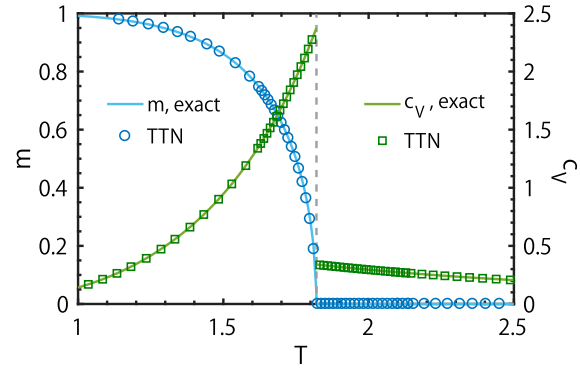

FIG. 13. Comparisons between the TTN calculations and the exact solution of the classical Ising model on the Bethe lattice, where a perfect agreement is seen in both the magnetic moment ($m = |\langle\sigma\rangle|$) and the specific heat c_V curves. The vertical dashed line denotes the critical temperature $T_c = 2/\ln(3)$.

It is also of interest to note, in Eq. (B5), that the spontaneous magnetization $m \sim (\frac{T_c - T}{T_c})^\kappa$ with $\kappa = 1/2$, when T approaches the transition temperature T_c (from low temperature side). In addition, the internal energy u_b curve is continuous at T_c, while the slope $c_V \equiv \partial u_b/\partial T$ shows a discontinuity in Fig. 13(b), suggesting a mean-field-type critical exponent $\alpha = 0$.

APPENDIX C: THE *r-q* TRANSFORMATION

Here we provide more details on the *r-q* transformations of the bilinear terms, including the hopping, on-site occupation number, pair-creation, or annihilation terms, etc.

First, we check that the real-space on-site term remains as on-site term in the q space

$$\begin{aligned} \sum_{R_l} a^\dagger_{R_l} a_{R_l} &= \sum_{R_l}\sum_{Q_l,Q_l'} a^\dagger_{Q_l}\left(\prod_{\lambda=1}^{l} U_{q_\lambda r_\lambda} U^\dagger_{r_\lambda q'_\lambda}\right) a_{Q_l'} \\ &= \sum_{Q_l,Q_l'} a^\dagger_{Q_l}\left(\prod_{\lambda=1}^{l}\sum_{r_\lambda} U_{q_\lambda r_\lambda} U^\dagger_{r_\lambda q'_\lambda}\right) a_{Q_l'} \\ &= \sum_{Q_l,Q_l'} a^\dagger_{Q_l} a_{Q_l'}\delta_{Q_l,Q_l'} = \sum_{Q_l} a^\dagger_{Q_l} a_{Q_l}. \end{aligned} \tag{C1}$$

For the NN hopping term, we have

$$\begin{aligned} \sum_{R_l,r_{l+1}} a^\dagger_{R_l} a_{R_l r_{l+1}} &= \sum_{R_l,r_{l+1}}\sum_{Q_l',Q_l,q_{l+1}} a^\dagger_{Q_l'}\prod_{\lambda=1}^{l} U_{q'_\lambda,r_\lambda}\prod_{\lambda=1}^{l+1} U^\dagger_{r_\lambda,q_\lambda}\, a_{Q_l q_{l+1}} \\ &= \sum_{r_{l+1}}\sum_{Q_l',Q_l,q_{l+1}} \delta_{Q_l',Q_l} a^\dagger_{Q_l'} U^\dagger_{r_{l+1},q_{l+1}} a_{Q_l q_{l+1}} \\ &= \sum_{Q_l,q,r}\frac{1}{\sqrt{\tilde z}} e^{-2\pi i q r/\tilde z} a^\dagger_{Q_l} a_{Q_l q} = \sqrt{\tilde z}\sum_{Q_l} a^\dagger_{Q_l} a_{Q_l 0}, \end{aligned} \tag{C2}$$

where $\tilde z = z - 1$ for $l > 1$ layers and $\tilde z = z$ for $l = 1$ one.

In the HAF model, we have pair-creation and annihilation operators, where additional care needs to be taken

of, i.e.,

$$a_{Q_l} = \begin{cases} \sum_{R_l} \left(\prod_{\lambda=1}^{l} U_{q_\lambda, r_\lambda}\right) a_{R_l}, & l \in \text{odd}, \\ \sum_{R_l} a_{R_l} \left(\prod_{\lambda=1}^{l} U^{\dagger}_{r_\lambda, q_\lambda}\right), & l \in \text{even}. \end{cases} \tag{C3}$$

Therefore, the pair creation and annihilation operators can be transformed into q space in a well organized way, e.g.,

$$\begin{aligned} \sum_{R_l, r_{l+1}} a_{R_l} a_{R_l r_{l+1}} &= \sum_{R_l, r_{l+1}} \sum_{Q'_l, Q_l, q_{l+1}} a_{Q'_l} \prod_{\lambda=1}^{l} U_{q'_\lambda, r_\lambda} \prod_{\lambda=1}^{l+1} U^{\dagger}_{r_\lambda, q_\lambda} a_{Q_l q_{l+1}} \delta_{l,\text{even}} + \sum_{R_l, r_{l+1}} \sum_{Q'_l, Q_l, q_{l+1}} \prod_{\lambda=1}^{l} U^{\dagger}_{r_\lambda, q_\lambda} a_{Q_l} a_{Q'_l, q'_{l+1}} \prod_{\lambda=1}^{l+1} U_{q'_\lambda, r_\lambda} \delta_{l,\text{odd}} \\ &= \sum_{r_{l+1}} \sum_{Q'_l, Q_l, q_{l+1}} \delta_{Q'_l, Q_l} a_{Q'_l} U^{\dagger}_{r_{l+1}, q_{l+1}} a_{Q_l q_{l+1}} \delta_{l,\text{even}} + \sum_{r_{l+1}} \sum_{Q'_l, Q_l, q_{l+1}} \delta_{Q'_l, Q_l} a_{Q_l} a_{Q'_l q'_{l+1}} U_{q'_{l+1}, r_{l+1}} \delta_{l,\text{odd}} \\ &= \sum_{Q_l, q, r} \frac{1}{\sqrt{\tilde{z}}} e^{-2\pi i q r/\tilde{z}} a_{Q_l} a_{Q_l q} \delta_{l,\text{even}} + \sum_{Q_l, q, r} \frac{1}{\sqrt{\tilde{z}}} e^{+2\pi i q r/\tilde{z}} a_{Q_l} a_{Q_l q} \delta_{l,\text{odd}} = \sqrt{\tilde{z}} \sum_{Q_l} a_{Q_l} a_{Q_l 0}, \end{aligned} \tag{C4}$$

which again falls into an effective 1D chain geometry.

APPENDIX D: THE BOGOLIUBOV TRANSFORMATION IN THE XY MODEL

In this Appendix we provide the details of the Bogoliubov transformation for the XY model. We start from the 1D half-chain bosonic Hamiltonian, i.e., Eq. (33) in the main text. By ignoring the "impurity site" at the center, performing a Fourier transformation on an infinite chain (without changing the energy dispersion curve), we arrive at $H_{1\text{D}} = \sum_{\kappa \geqslant 0} H_\kappa$, where

$$H_\kappa = S[(z + \gamma_\kappa)(b^{\dagger}_\kappa b_\kappa + b^{\dagger}_{-\kappa} b_{-\kappa}) + \gamma_\kappa (b_\kappa b_{-\kappa} + b^{\dagger}_\kappa b^{\dagger}_{-\kappa})], \tag{D1}$$

with $\gamma_\kappa = \sqrt{z-1}\cos\kappa$.

The sub-Hamiltonian H_κ can be rewritten as $H_\kappa = \frac{1}{2} B^{\dagger} \mathcal{H}_\kappa B$, where $B = (b_\kappa, b_{-\kappa}, b^{\dagger}_\kappa, b^{\dagger}_{-\kappa})^T$ and

$$\mathcal{H}_\kappa = S \begin{pmatrix} z+\gamma_\kappa & & & \gamma_\kappa \\ & z+\gamma_\kappa & \gamma_\kappa & \\ & \gamma_\kappa & z+\gamma_\kappa & \\ \gamma_\kappa & & & z+\gamma_\kappa \end{pmatrix}, \tag{D2}$$

where we have omitted the term $-(z + \gamma_\kappa)$ which is a constant after summing over κ.

In the Bogoliubov transformation, we find a matrix Θ so that (1) $B = \Theta \tilde{B}$, where $\tilde{B} = (\beta_\kappa, \beta_{-\kappa}, \beta^{\dagger}_\kappa, \beta^{\dagger}_{-\kappa})^T$ still represents boson operators obeying the bosonic statistics, and (2) $H_\kappa = \frac{1}{2} \tilde{B}^{\dagger} \Theta^{\dagger} \mathcal{H}_\kappa \Theta \tilde{B} = \frac{1}{2} \tilde{B}^{\dagger} \mathbf{D} \tilde{B}$ is in a diagonal form.

To maintain the boson statistics in condition (1), we require $\Theta^{\dagger} \Lambda_z \Theta = \Lambda_z$, where

$$\Lambda_z = \begin{pmatrix} \mathbf{I}_{2\times 2} & \\ & -\mathbf{I}_{2\times 2} \end{pmatrix},$$

and $\mathbf{I}_{2\times 2}$ is a 2×2 identity matrix.

Combing together conditions (1) and (2), we have $(\Lambda_z \mathcal{H}_\kappa)\Theta = \Theta \Lambda_z \Theta^{\dagger} \mathcal{H}_\kappa \Theta = \Theta \Lambda_z \mathbf{D}$, which implies Θ and $\mathbf{D}$ can be found by diagonalizing $\Lambda_z \mathcal{H}_\kappa$. After some calculations, and by observing that the Hamiltonian matrix in Eq. (D2) is block diagonal, we arrive at

$$(\tilde{\epsilon}/S)^2 - (z + \gamma_\kappa)^2 + \gamma_\kappa^2 = 0,$$

where the positive root with $\kappa > 0$ constitutes the magnon spectrum in Eq. (34), i.e., $\epsilon(\kappa) = \tilde{\epsilon}(\kappa)$. The corresponding Bogolon (annihilation) operator turns out to be

$$\beta_\kappa = \cosh(\theta_\kappa) b_\kappa - \sinh(\theta_\kappa) b^{\dagger}_{-\kappa}, \tag{D3}$$

with restriction $\kappa \in [0, \pi]$, where θ_κ can be determined from $\tanh(\theta_\kappa) = -\gamma_\kappa/(z + \gamma_\kappa)$.

[1] H. A. Bethe, Statistical theory of superlattices, Proc. R. Soc. London Ser. A **150**, 552 (1935).

[2] R. K. Pathria and P. D. Beale, *Statistical Mechanics*, 3rd ed. (Academic, New York, 2011).

[3] M. Ostilli, Cayley trees and Bethe lattices: A concise analysis for mathematicians and physicists, Physica A **391**, 3417 (2012).

[4] M. Eckstein, M. Kollar, K. Byczuk, and D. Vollhardt, Hopping on the Bethe lattice: Exact results for densities of states and dynamical mean-field theory, Phys. Rev. B **71**, 235119 (2005).

[5] O. Petrova and R. Moessner, Coulomb potential $V(r) = 1/r$ problem on the Bethe lattice, Phys. Rev. E **93**, 012115 (2016).

[6] G. Semerjian, M. Tarzia, and F. Zamponi, Exact solution of the Bose-Hubbard model on the Bethe lattice, Phys. Rev. B **80**, 014524 (2009).

[7] H. C. Jiang, Z. Y. Weng, and T. Xiang, Accurate Determination of Tensor Network State of Quantum Lattice Models in two Dimensions, Phys. Rev. Lett. **101**, 090603 (2008).

[8] F. Verstraete, V. Murg, and J. I. Cirac, Matrix product states, projected entangled pair states, and variational renormalization group methods for quantum spin systems, Adv. Phys. **57**, 143 (2008).

[9] R. Orús, A practical introduction to tensor networks: Matrix product states and projected entangled pair states, Ann. Phys. **349**, 117 (2014).

[10] W. Li, J. von Delft, and T. Xiang, Efficient simulation of infinite tree tensor network states on the Bethe lattice, Phys. Rev. B **86**, 195137 (2012).

[11] W. Li, S.-S. Gong, Y. Zhao, and G. Su, Quantum phase transition, $O(3)$ universality class, and phase diagram of the spin-$\frac{1}{2}$ Heisenberg antiferromagnet on a distorted honeycomb lattice: A tensor renormalization-group study, Phys. Rev. B **81**, 184427 (2010).

[12] T. Liu, S.-J. Ran, W. Li, X. Yan, Y. Zhao, and G. Su, Featureless quantum spin liquid, $\frac{1}{3}$-magnetization plateau state, and exotic thermodynamic properties of the spin-$\frac{1}{2}$ frustrated Heisenberg antiferromagnet on an infinite Husimi lattice, Phys. Rev. B **89**, 054426 (2014).

[13] T. Liu, W. Li, A. Weichselbaum, J. von Delft, and G. Su, Simplex valence-bond crystal in the spin-1 kagome Heisenberg antiferromagnet, Phys. Rev. B **91**, 060403(R) (2015).

[14] T. Liu, W. Li, and G. Su, Spin-ordered ground state and thermodynamic behaviors of the spin-$\frac{3}{2}$ kagome Heisenberg antiferromagnet, Phys. Rev. E **94**, 032114 (2016).

[15] H. Otsuka, Density-matrix renormalization-group study of the spin-1/2 XXZ antiferromagnet on the Bethe lattice, Phys. Rev. B **53**, 14004 (1996).

[16] B. Friedman, A density matrix renormalization group approach to interacting quantum systems on Cayley trees, J. Phys.: Condens. Matter **9**, 9021 (1997).

[17] M. Kumar, S. Ramasesha, and Z. G. Soos, Density matrix renormalization group algorithm for Bethe lattices of spin-$\frac{1}{2}$ or spin-1 sites with Heisenberg antiferromagnetic exchange, Phys. Rev. B **85**, 134415 (2012).

[18] H. J. Changlani, S. Ghosh, C. L. Henley, and A. M. Läuchli, Heisenberg antiferromagnet on Cayley trees: Low-energy spectrum and even/odd site imbalance, Phys. Rev. B **87**, 085107 (2013).

[19] H. J. Changlani, S. Ghosh, S. Pujari, and C. L. Henley, Emergent Spin Excitations in a Bethe Lattice at Percolation, Phys. Rev. Lett. **111**, 157201 (2013).

[20] W. F. Brinkman and T. M. Rice, Single-particle excitations in magnetic insulators, Phys. Rev. B **2**, 1324 (1970).

[21] R. C. Kittler and L. M. Falicov, Electronic structure of disordered binary alloys, J. Phys. C: Solid State Phys. **9**, 4259 (1976).

[22] F. Brouers and U. M. B. Marconi, On the antiferromagnetic phase in the Hubbard model, J. Phys. C: Solid State Phys. **15**, L925 (1982).

[23] M. A. Hajj, N. Guihéry, J.-P. Malrieu, and P. Wind, Theoretical studies of the phase transition in the anisotropic two-dimensional square spin lattice, Phys. Rev. B **70**, 094415 (2004).

[24] S. R. White, Density Matrix Formulation for Quantum Renormalization Groups, Phys. Rev. Lett. **69**, 2863 (1992).

[25] G. Vidal, Classical Simulation of Infinite-size Quantum Lattice Systems in one Spatial Dimension, Phys. Rev. Lett. **98**, 070201 (2007).

[26] R. Orús and G. Vidal, Infinite time-evolving block decimation algorithm beyond unitary evolution, Phys. Rev. B **78**, 155117 (2008).

[27] W. Li, S.-J. Ran, S.-S. Gong, Y. Zhao, B. Xi, F. Ye, and G. Su, Linearized Tensor Renormalization Group Algorithm for the Calculation of Thermodynamic Properties of Quantum Lattice Models, Phys. Rev. Lett. **106**, 127202 (2011).

[28] Y.-L. Dong, L. Chen, Y.-J. Liu, and W. Li, Bilayer linearized tensor renormalization group approach for thermal tensor networks, Phys. Rev. B **95**, 144428 (2017).

[29] S.-J. Ran, W. Li, B. Xi, Z. Zhang, and G. Su, Optimized decimation of tensor networks with super-orthogonalization for two-dimensional quantum lattice models, Phys. Rev. B **86**, 134429 (2012).

[30] B.-B. Chen, Y.-J. Liu, Z. Chen, and W. Li, Series-expansion thermal tensor network approach for quantum lattice models, Phys. Rev. B **95**, 161104(R) (2017).

[31] B.-B. Chen, L. Chen, Z. Chen, W. Li, and A. Weichselbaum, Exponential Thermal Tensor Network Approach for Quantum Lattice Models, Phys. Rev. X **8**, 031082 (2018).

[32] P. Czarnik, L. Cincio, and J. Dziarmaga, Projected entangled pair states at finite temperature: Imaginary time evolution with ancillas, Phys. Rev. B **86**, 245101 (2012).

[33] P. Czarnik and J. Dziarmaga, Variational approach to projected entangled pair states at finite temperature, Phys. Rev. B **92**, 035152 (2015).

[34] P. Czarnik, M. M. Rams, and J. Dziarmaga, Variational tensor network renormalization in imaginary time: Benchmark results in the Hubbard model at finite temperature, Phys. Rev. B **94**, 235142 (2016).

[35] P. Czarnik, J. Dziarmaga, and A. M. Oleś, Overcoming the sign problem at finite temperature: Quantum tensor network for the orbital e_g model on an infinite square lattice, Phys. Rev. B **96**, 014420 (2017).

[36] A. Kshetrimayum, M. Rizzi, J. Eisert, and R. Orús, Tensor Network Annealing Algorithm for Two-dimensional Thermal States, Phys. Rev. Lett. **122**, 070502 (2019).

[37] P. Czarnik, J. Dziarmaga, and P. Corboz, Time evolution of an infinite projected entangled pair state: An efficient algorithm, Phys. Rev. B **99**, 035115 (2019).

[38] P. Czarnik and P. Corboz, Finite correlation length scaling with infinite projected entangled pair states at finite temperature, Phys. Rev. B **99**, 245107 (2019).

[39] T. Prosen and I. Pižorn, Operator space entanglement entropy in a transverse Ising chain, Phys. Rev. A **76**, 032316 (2007).

[40] T. Barthel, One-dimensional quantum systems at finite temperatures can be simulated efficiently on classical computers, arXiv:1708.09349.

[41] J. Dubail, Entanglement scaling of operators: a conformal field theory approach, with a glimpse of simulability of long-time dynamics in 1 + 1d, J. Phys. A: Math. Theor. **50**, 234001 (2017).

[42] L. Chen, D.-W. Qu, H. Li, B.-B. Chen, S.-S. Gong, J. von Delft, A. Weichselbaum, and W. Li, Two-temperature scales in the triangular-lattice Heisenberg antiferromagnet, Phys. Rev. B **99**, 140404(R) (2019).

[43] N. D. Mermin and H. Wagner, Absence of Ferromagnetism or Antiferromagnetism in One- or Two-Dimensional Isotropic Heisenberg Models, Phys. Rev. Lett. **17**, 1133 (1966).

[44] C. R. Laumann, S. A. Parameswaran, and S. L. Sondhi, Absence of Goldstone bosons on the Bethe lattice, Phys. Rev. B **80**, 144415 (2009).

[45] M.-B. Lepetit, M. Cousy, and G. M. Pastor, Density-matrix renormalization study of the Hubbard model on a Bethe lattice, Eur. Phys. J. B **13**, 421 (2000).

[46] G. D. Mahan, Energy bands of the Bethe lattice, Phys. Rev. B **63**, 155110 (2001).

[47] R. J. Baxter, *Exactly Solved Models in Statistical Mechanics* (Courier Corporation, North Chelmsford, MA, 2013).

[48] M. Mézard and G. Parisi, The Bethe lattice spin glass revisited, Eur. Phys. J. B **20**, 217 (2001).